Experimental study of the upstream bathymetry effects on a ducted twin vertical axis turbine

Moreau Martin [1, 2], Bloch Noam [1], Germain Grégory [1, *], Maurice Guillaume [2]

[1] Ifremer, Marine Structure Laboratory, 150 Quai Gambetta, 62200 Boulogne sur Mer, France
[2] HydroQuest SAS, 16 Chemin de Malacher, 38240 Meylan, France

* Correponding author : Grégory Germain, email address : gregory.germain@ifremer.fr

Abstract :

Tidal turbines at sea are subject to complex flow conditions. Among that complexity, wide bathymetry obstacles can generate powerful coherent flow structures whose impact on horizontal axis tidal turbines was proved to be highly detrimental. Consequently, the present paper aims at studying the effects of such coherent flow structures on the response of another tidal turbine geometry, namely a bottom-mounted ducted twin vertical axis tidal turbine (2-VATT). We tested a 1/20 scale model of such a 2-VATT in Ifremer's flume tank either with a flat bed or downstream of a wide bathymetry obstacle at a constant far upstream velocity and we measured the turbine response simultaneously with the flow velocity. These flow measurements make it possible to compute cross-correlations in order to analyse the influence of the velocity fluctuation on the turbine response. The results reveal a strong drop in the average power and loads coefficients of the 2-VATT combined with significantly larger fluctuation. The velocity deficit and the high level of turbulence in the obstacle wake is responsible for a 40 % lower average power coefficient and more than 3 times higher standard deviation compared to the flat bed configuration. The loads standard deviations are multiplied by 2 for the drag and by 10 for the lift when the 2-VATT is downstream of the bathymetry obstacle. This behaviour strongly increases the risks of structural fatigue failure, but the turbine drifting or overturning risks under those conditions remain lower than with the flat bed. The power fluctuation increase appears to be mostly due to the flow shear in the obstacle wake whereas the load fluctuation is mostly due to the periodical passing of the coherent flow structures. Thus, a proper characterisation of the flow at each precise turbine locations prior deployment at sea is highly recommended to design their structure accordingly.

Highlights

► Vertical axis turbine in the wake of uneven bathymetry generating flow variation. ► Obstacle wake induces strong drop in the average power and loads coefficients. ► Sheared flow and turbulence extend the torque and power fluctuations. ► Coherent flow structures induce load fluctuations.

Nomenclature

c	Blade chord
G0	Test configuration with a flat floor
C6	Test configuration with a bathymetry obstacle
C_{Pcol}	Power coefficient of one rotor column
C_P	Total power coefficient
D	Rotor diameter
FI	Fluctuation Intensity (standard deviation divided by average)
$F.$	Force measured below the turbine with the subscript indicating the direction
f_u	Vortex shedding frequency behind the bathymetry obstacle
f_ω	Rotor's rotational frequency
h	Height of the square cylinder bathymetry obstacle
H	Capture height of the turbine
H_{blade}	Rotor blade height
HATT	Horizontal Axis Tidal Turbine
λ_{opt}	Tip speed ratio providing the maximal power coefficient
LDV	Laser Doppler Velocimetry with 2 (u_{2C},v_{2C}) or 3 (u_{3C},v_{3C},w_{3C}) velocity Components
$M.$	Moment measured below the turbine base with the subscript indicating the direction
PDF	Probability Density Function
Q	Torque of a rotor column
R	Rotor radius
$\mathcal{R}$	Cross-correlation coefficient
σ	Standard deviation
$\mathcal{S}$	Power spectral density
TI_u	Streamwise turbulence intensity
U_0	Far upstream streamwise velocity measured at the centre of the projected capture area of the 2-VATT
U_S	Surface averaged streamwise velocity over the capture area at the turbine location before its installation
2-VATT	Twin Vertical Axis Tidal Turbine
ω	Rotational speed
W	Turbine width
$\overline{\square}$	Arithmetic average of the quantity below the bar

1   Introduction

Sea sites identified for potential tidal turbine installations are characterised by complex current conditions including high velocities with vertically sheared velocity profiles and turbulent flows, flow direction variability and surface waves (Gooch et al. 2009; Furgerot et al. 2020; Cossu et al. 2021). Amongst this complexity, Mercier et al. 2021 and Mercier et al. 2022 found a high spatial variability of the tidal streams characteristics over distances of less than 100 m and over short time scales at the Paimpol-Bréhat test site, France. In addition, they observed that large bathymetric singularities generate highly energetic coherent flow structures with a rising trajectory from the sea bed to the free surface, generating boils in the Alderney Race, France. Coherent turbulent structures were also measured at the Fall of Warness, Scotland, by Naberezhnykh et al. 2023, and in the Menai Straits, Wales, by Lucas et al. 2022 where the most powerful coherent structures have a median length-scale of 13.2 m with a periodicity of about 105 s. Specific studies have been carried out in Ifremer's wave and current tank to reproduce such flow configurations at a 1/20 scale and to better understand the flow disturbances induced by bathymetry obstacles (Ikhennicheu et al. 2019a; Magnier et al. 2021). Among the diversity of obstacles studied, a generic wide bottom mounted square cylinder of base $h \times h$ and width

$6h$, with $h = 0.25$ m, was found to reproduce those highly energetic coherent flow structures with a rising trajectory (Ikhennicheu et al. 2019b; Mercier et al. 2020).

The vortices are shed in the cylinder wake with a Strouhal number $St = f_u h/U \simeq 0.062$, with f_u the vortex shedding frequency and U the far upstream velocity, and their diameter was estimated to be about 0.6 m using Lamb-Osen vortex profiles. Thus, the coherent flow structures past the wide bottom mounted cylinder are of the same order of magnitude, both in time and space, as coherent structures measurement at sea according to Reynolds number similitude law (Lucas et al. 2022). Knowing the effect of such flow structures on tidal turbines located on their path is crucial for an appropriate structural design (Milne et al. 2010; Thiébaut et al. 2020).

Chamorro et al. 2015 first tested experimentally a Horizontal Axis Tidal Turbine (HATT) in the wake of vertically oriented cylinders. They found a strong interaction between the large-scale and broadband turbulence shed by the cylinders and the turbine power production. Then, Ouro et al. 2019 modelled the effect of sharp dunes on another HATT using large eddy simulations (LES). Their results provide quantitative evidence of the effect of seabed-induced turbulence on the instantaneous performance and structural loadings of the turbine revealing how large-scale, energetic turbulence structures affect the turbine performance. They also show that turbine wake recovery is enhanced compared to the same turbine operating above a flat bathymetry due to the higher turbulence levels. Furthermore, Gaurier et al. 2020a; Gaurier et al. 2020b tested Ifremer's generic HATT in the wake of the above mentioned wide bottom mounted square cylinder. They reveal large blade root force fluctuation due to the rotation through the sheared velocity field and show that the turbine load fluctuation directly responds to the vortex shedding low frequency f_u. Based on the same database, Druault et al. 2022 explains that the typical turbine power frequency spectra decay in the inertial range (proportional to a -11/3 power law) is due to the spatial averaging of the velocity spectrum by the turbine blades. However, those studies only focus on HATT while Vertical Axis Tidal Turbines (VATT) are also good candidates for tidal energy harvesting due to their performance insensitivity to the flow direction among other advantages (Ouro et al. 2022).

To the authors knowledge, the effect of coherent flow structures on VATT have not been studied yet. However, experiments were carried out to analyse the effect of ambient turbulence intensity on H-rotor vertical axis wind turbines (Ahmadi-Baloutaki et al. 2015; Möllerström et al. 2016). The results show that the power performance only slightly increases with the turbulence intensity from 5 to more than 15 %, with variable results depending on the reference velocity computation method. In addition, coupled wind tunnel tests and large eddy simulations on a straight-bladed vertical axis wind turbine showed that grid turbulence benefited both self-starting and wake recovery with a greater power production in turbulent flows (Peng et al. 2016). Grondeau et al. 2019 also used LES (with lattice Boltzmann actuator-line approach) to model the wake of a ducted twin-vertical axis tidal turbine (2-VATT) similar to *HydroQuest*'s 1 MW-rated demonstrator (Moreau et al. 2022) with several upstream turbulence intensities. Their results show that the turbulence not only enhances the wake recovery but also modifies the wake shape evolution with the downstream distance. Besides, the effect of an undisturbed sheared flow on that same ducted 2-VATT at a 1/20 scale was analysed experimentally and was found to strongly increase the power fluctuation without affecting the average performance (Moreau et al. 2023b). Finally, the authors tested that ducted 2-VATT in the wake of two bathymetry obstacle configurations amongst those of Ikhennicheu et al. 2019a and Magnier et al. 2021 with two turbine-to-obstacle distances for each obstacle (Bloch et al. 2022). They found that the ducted 2-VATT power and load fluctuation is strongly increased compared to a flat bathymetry configuration, with a variable intensity depending on the obstacle shape and relative distance to the turbine. However, that study focused on the 2-VATT response alone and lacks the analysis of the flow measurements to further explain and discuss the results observed.

3

So, the aim of the present paper is to compare experimentally the behaviour of the ducted 2-VATT between a flat bed configuration and the most impacting bathymetry obstacle configuration found by Bloch et al. 2022 to deeper investigate the effects of that particular flow on the turbine power generation and on the loads. To do so, the section 2 first describes the turbine model (2.1) as well as the flat bed and the uneven bathymetry setups (2.2) before describing the flow characteristics in these two configurations (2.3) and the data processing carried out (2.4). Then, the section 3 presents the effects of the bathymetry obstacle wake on the 2-VATT power performance (3.1) and on its loads (3.2). Finally, the study shines a light on the interaction between the flow fluctuation induced by the coherent structures shed in the bathymetry obstacle wake and the 2-VATT response (3.3).

2 Material and method

First, this section aims at describing the ducted twin vertical axis tidal turbine model, the instrumentation used and their setup in the tank. Then, we describe the upstream flow characteristics either with the flat floor or with the bottom mounted bathymetry obstacle before describing the data processing carried out for this study.

2.1 Turbine model

The ducted 2-VATT 1/20 scale model is geometrically similar to the 1 MW-rated demonstrator tested by *HydroQuest* at the Paimpol-Bréhat test site from 2019 to 2021 (Moreau et al. 2022). It is composed of two independent counter-rotating vertical axis rotor columns, like shown in Fig. 1.
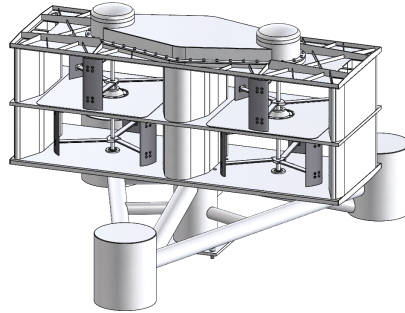

Figure 1: CAD view of the ducted 2-VATT 1/20 scale model.

Each column is made of two levels of H-Darrieus type rotors fixed to the same shaft with a 60° phase difference between the levels. Besides, each rotor of radius $R = D/2 = 200$ mm is made of $N = 3$ blades that are $H_{blade} = 190$ mm high with a chord c of 73 mm. Thus, the rotor solidity (Nc/R) is 1.1. The rotors are mounted in a $W = 1.24$ m wide structure made of fairings and plates. The turbine height is defined as the distance between the top and the bottom horizontal plates such that $H = 450$ mm; and the 2-VATT capture area is $H \times W$. The two rotor columns are controlled at a constant rotational speed by two independent *Maxon RE50* DC motors and *Escon 70/10* servo-controllers. The torque Q of each rotor column is measured using *Scaime DR2112-W* torque-meters and the rotational speeds ω are measured by the motor encoders. The turbine is fixed on a pseudo-tripod base through a 6-component load cell (*SIXAXES* 1.5 kN) to measure the loads on the turbine alone. The model is fixed to the tank floor at the bottom of the central pile of the base on another 6-component load

cell (*SIXAXES* 20 kN) to measure the overall loads on the turbine and the base. All of these analogue signals are acquired at a sampling frequency of 128 Hz using *National Instruments PXI* and *LabView* systems. The model and its instrumentation are fully described in Moreau et al. 2023a.

Whether the flow comes from one side or the other of the device, the base geometry upstream and the relative counter-rotation direction of the two column reverses. The two flow directions are referred to either as FC, corresponding to the Flood tide Configuration at the Paimpol-Bréhat test site, or as EC for the Ebb tide Configuration (Fig. 2).
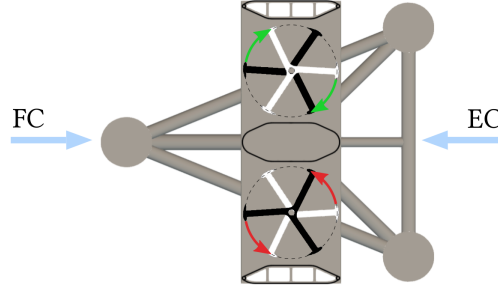
Figure 2: Schematic top view of the turbine with the two flow directions representing Flood and Ebb tide Configurations.

2.2 Experimental setup

The 2-VATT model was tested in the Ifremer's 2 m deep and 4 m wide wave and current flume tank in Boulogne-sur-mer, France (Gaurier et al. 2018). It is operated in its low turbulence configuration with the inlet conditioned by a honeycomb structure and a uniform grid. The flood and ebb tide relative flow directions are modelled by turning 2-VATT around as the flume tank allows a single flow direction. We used two experimental setups to assess the effect of the bathymetry obstacle wake on the behaviour of the 2-VATT compared to the case without obstacle. The 2-VATT is placed at the centre of the tank $(x, y, z) = (0, 0, 0)$ with x in the main flow direction, y towards the wall and z towards the free surface. The first configuration models a flat bathymetry and is referred to as G0 (Fig. 3). In that case, a *Dantec* 2-Component Laser Doppler Velocimeter (2C-LDV) measures the velocities (u, v) along (x, y) at $x = -6H$ at the centre of the turbine capture area, ie. $(y, z) = (0, 0.505)$ m. At this far upstream distance, the flow is not disturbed by the 2-VATT (Moreau et al. 2023a). The time average of u at this location is considered as the reference far upstream velocity and is noted U_0. The 2C-LDV and the turbine related signals are acquired simultaneously during 3 minutes to guarantee the time convergence of the average and the standard deviation of the signals.

The second setup models a strong bathymetry variation upstream of the turbine and is referred to as C6 (Fig. 4 and 5). The wide square base cylinder of size $6h \times h \times h$ studied by Ikhennicheu et al. 2019b is placed 10 obstacle heights upstream of the 2-VATT ($x = -10h$). We placed two LDV devices at $x = -H$ to measure the flow velocity right in front of the 2-VATT. The 2C-LDV measures (u_{2C}, v_{2C}) at the centre of the top rotor at $(y, z) = (0.31, 0.61)$ m and a *Dantec* 3C-LDV measures (u_{3C}, v_{3C}, w_{3C}) in front of the bottom rotor at $(y, z) = (0.31, 0.41)$ m. The LDV measurements are in front of the red column in FC and in front on the green column in EC (Fig. 2). The two LDV probes and the turbine related signals are acquired simultaneously during 5 minutes to guarantee the time convergence of the average and the standard deviation of the signals.

In the two setups, the tank operates at the same velocity setpoint of 1 m.s^{-1} which, gives a blade chord based Reynolds number ($Re_c = \frac{c\lambda U_0}{\nu}$, with ν the water kinematic viscosity and λ the
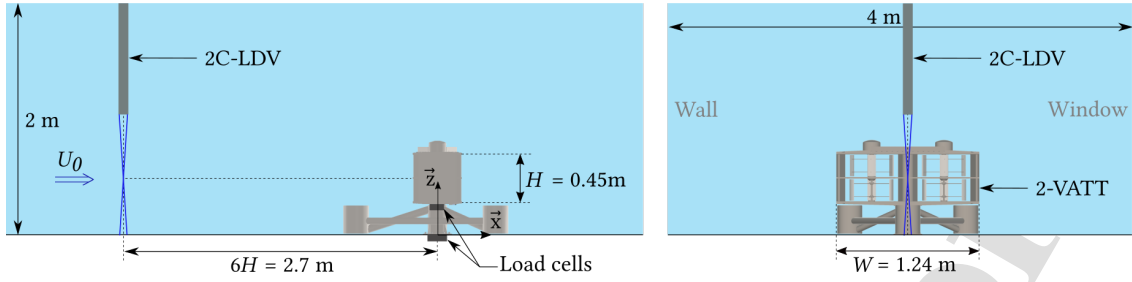
5

Figure 3: Schematic side view (left) and front view (right) of the experimental setups in the G0 configuration.
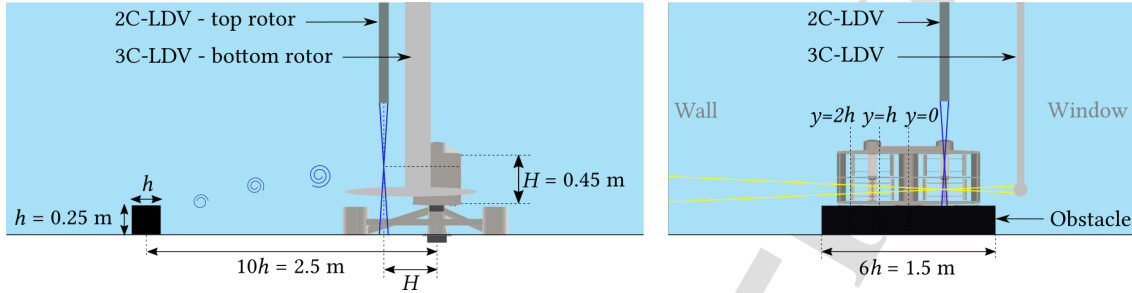

Figure 4: Schematic side view (left) and front view (right) of the experimental setups in the C6 configuration.

tip speed ratio - Eq. 3) of the order of 10^5; the two rotor columns are controlled separately with the same constant rotational speed setpoint; and the LDV devices operate in non-coincident mode, meaning that the different velocity components are measured independently by each pair of lasers. The data rate for each velocity component is of the order of 200 Hz. The projected surface blockage of the bathymetry obstacles is 4.6 %, while it is close to 12 % with the 2-VATT (with or without the obstacle).
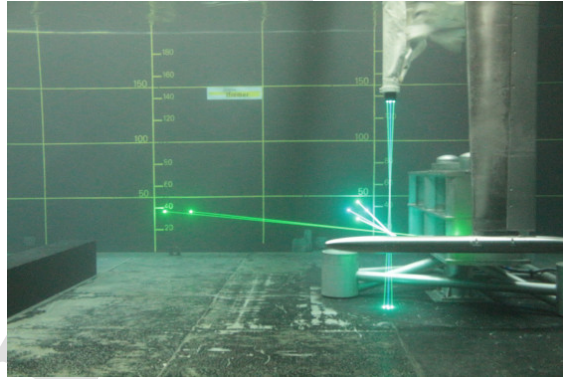

Figure 5: 2C- and 3C-LDV measurement between the bathymetry obstacle and the ducted 2-VATT model in the Ifremer's tank.

2.3 Flow characteristics

To compare the 2-VATT behaviour in one or the other flow configurations, it is necessary to characterise the flow beforehand, similarly to a resource assessment within the framework of a

6

full-scale turbine installation at sea. The flow characteristics in the empty tank, corresponding to the G0 configuration have already been characterised extensively. Gaurier 2020 shows that the flow characteristics are uniform over the tank width, so the velocity profiles measured with the 3C-LDV at the tank centre by Moreau et al. 2023a can be extruded along y (Fig. 6). Above the 0.3 m high boundary layer, the streamwise average velocity profile is uniform over the 2-VATT height and the streamwise turbulence intensity is about 1.5 %. The later is defined as $TI_u = \sigma(u)/\overline{u}$ with σ indicating the standard deviation and the bar indicating the time average. The transverse velocity components (v, w) are negligible.

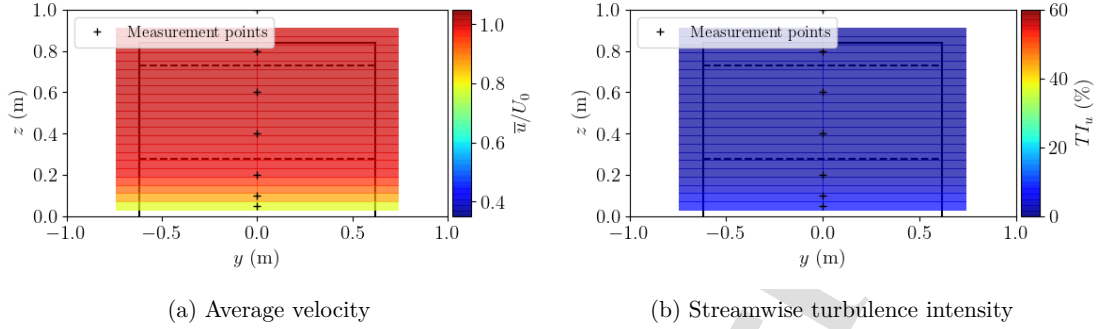(a) Average velocity   (b) Streamwise turbulence intensity

Figure 6: Streamwise average velocity (a) and turbulence intensity (b) profiles measured with the 3C-LDV at the centre of the empty tank and extruded along the y axis. The black lines represent the overall boundaries of the 2-VATT (absent during those measurements) and the dashed lines its capture area. The colour scales are the same as in Fig. 8 for comparison.

Regarding the C6 configuration, Ikhennicheu et al. 2019b showed no blockage effect of the obstacle on the far upstream velocity and characterised the turbulent wake of the wide bathymetry obstacle extensively using PIV measurements in the Ifremer wave and current flume tank. Fig. 7 displays the average streamwise and vertical velocity contours in the wake of the obstacle alone in (x, z) planes at the three lateral positions $y = 0$, h and $2h$ illustrated on the scheme in Fig. 4. The wake evolution appears to be fully three-dimensional with a recirculation zone, where $\overline{u} < 0$, extending down to $x = 6h$ at $y = 0$ and to $x = 4.5h$ at $y = 2h$, followed by a strong velocity gradient downstream. Besides, the turbulence characteristics of that specific flow were analysed both experimentally and numerically (Ikhennicheu et al. 2019b; Mercier et al. 2020). Thus, the turbine placed $10h$ downstream of the obstacle is out of the recirculation zone, in the sheared layer and on the coherent turbulent structures path. For the present study, we also mapped the flow similarly to a resource assessment at sea (without turbine) using the 3C-LDV in a (y, z) plane $8.2h$ downstream of the obstacle, i.e. at $x = -H$ which is the same position as the LDV measurements in front of the turbine in operation. Fig. 8(a) presents the average velocity field in the (y, z) plane with $\overline{u}/U_0$ in colour and $(\overline{v}, \overline{w})$ as an arrow field; and Fig. 8(b) presents the streamwise turbulence intensity with the location of the 3C-LDV measurement points. The measurements along the profile at $y = +0.31$ m are the same as at $y = -0.31$ m so we display the y-positive side as a symmetry of the negative side. The maps are obtained by linear interpolation between the measurement points with a 40 mm step in the y and z directions. The wide bathymetry obstacle is represented by the grey filled rectangle and the 2-VATT overall boundaries are represented by the black lines to illustrate the relative flow scale, even though the turbine was absent during this flow characterisation. The average velocity map reveals a strong flow shear with a maximum of 45 % difference between the top of the turbine capture height ($z = 0.73$ m) and its bottom ($z = 0.28$ m) at the centre of the tank and an average difference over the turbine width of 34 %. In addition, the transverse velocities appear to be significant as $\overline{v}$ ranges in $\pm$ 0.13 U_0 and $\overline{w}$, mostly towards the tank
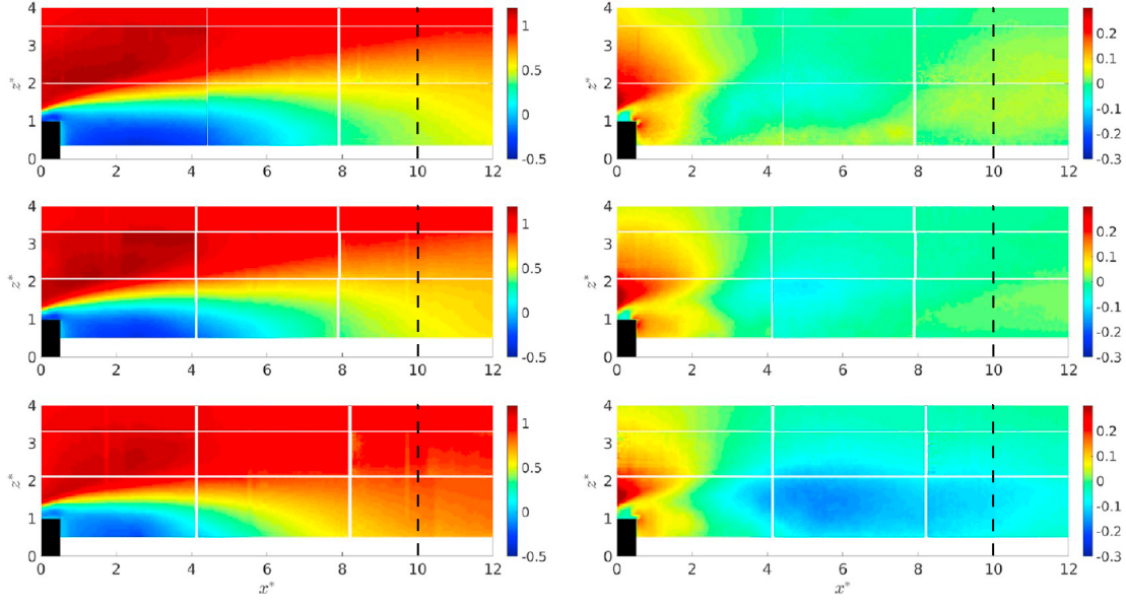
7

Figure 7: Average streamwise velocity (left) and vertical velocity fields (right) from PIV measurements in the wake of the square cylinder (black), both normalised by the far upstream average streamwise velocity, from Ikhennicheu et al. 2019b. $x^* = x/h$ is the streamwise direction, $z^* = z/h$ is the vertical one and y is the transverse one. The top figures are at $y = 0$, the tank and the obstacle centre, the middle figures are at $y = h$ and the bottom ones at $y = 2h$ (Fig. 4). The dashed lines display the 2-VATT centre location in the C6 test configuration.

bottom, ranges in $[-0.10; 0.07]U_0$. The average kinetic energy loss due to the velocity deficit in the cylinder wake is compensated by an increase of the turbulent kinetic energy. Thus, the turbulence intensity is also at its maximum at the centre of the obstacle wake with 54 % at the bottom of the turbine capture height and 20 % at the top. The average TI_u over the 2-VATT capture area is about 27 %.

The difference of turbulence levels between the configurations G0 and C6 is clearly depicted by the probability density functions of the streamwise velocity measured at $(x, y, z) = (0, 0, 0.6)$ m without turbine in the two configurations (Fig. 9). Indeed, at that location, the normalised velocity values range from 0.94 to 1.08 in the flat bed configuration whereas they range from -0.22 to 1.55 in the cylinder wake. Furthermore, the flow measurements in the flat bed configuration and in the wake of the bathymetric obstacle are presented in the spectral domain in Fig. 10. Power spectral densities of the fluctuating part of u, $\mathcal{S}(u'/U_0)$, are computed using Welch's method with 64 s long windows and 50 % overlap. Several observations can be made. Firstly, the level of energy at the centre of the tank in the cylinder wake is about 100 times higher than without obstacle on the whole frequency range. That level of energy is constant between $y/h = \pm 1$ and decreases away from the tank centre. Secondly, the spectra behind the obstacle present a peak around $f_u = 0.25$ Hz, indicated by the vertical dashed line, which was found to be the shedding frequency of large coherent flow structures (Ikhennicheu et al. 2019b). That peak is the strongest at the tank centre ($y = 0$) at the two altitudes. However, it is almost absent at $y/h = 1$ and 2 at $z = 610$ mm whereas the peak remains marked at all the lateral positions at $z = 410$ mm. This result suggests that the bottom rotors of the 2-VATT will face wider coherent structures than the top ones. The energy peak at f_u appears again at $y/h = 3$, downstream of the lateral edge of the obstacle, only with 30 to 50 times less energy than at $y/H = 0$.

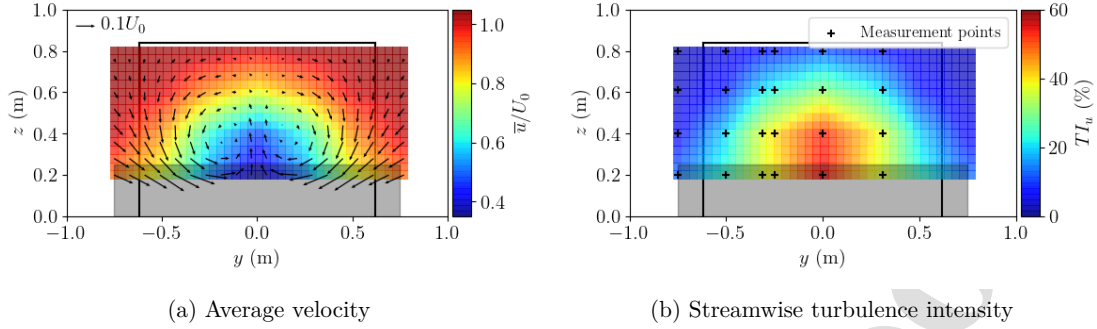(a) Average velocity

(b) Streamwise turbulence intensity

Figure 8: Downstream view of the 3C-LDV measurements in the wake of the obstacle without turbine at $x = -H$. (Left) Average streamwise velocity map with transverse velocities (v, w) arrow field. (Right) Streamwise turbulence intensity and position of the measurement points. The y-positive side is obtained by symmetry. The grey filled rectangle represents the obstacle and the black lines represent the overall boundaries of the 2-VATT (absent during the measurements).
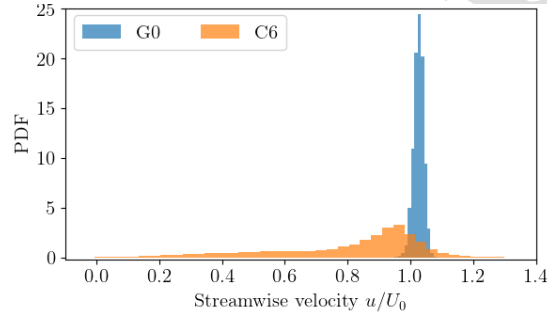

Figure 9: Probability density function (PDF) of the streamwise velocity measured by the 3C-LDV at $(x, y, z) = (0, 0, 0.6)$ m without turbine in the empty tank (G0) and in the wake of the bottom-mounted cylinder (C6).

2.4 Data processing

To compute the hydrodynamic coefficients, we consider two reference velocities: U_0, the time averaged far upstream velocity at the mid-height of the turbine, as defined in the Section 2.2, and U_S, the time and space averaged velocity at the turbine position without turbine, averaged over the capture area. Defined that way, U_0 is equivalent to the velocity measured upstream while operating a turbine at sea whereas U_S represents the velocity measured during a resource assessment prior turbine installation. The far upstream velocity U_0 is considered the same for the configurations G0 and C6 as the tank operates at the same velocity setpoint. In G0, the flow being homogeneous on the tank width (Gaurier 2020), U_S is obtained by extruding the velocity profile on the turbine width (Fig. 6). This method is similar to the one used with acoustic Doppler current profilers at sea for the certification of full scale tidal turbine performance according to the Technical Standard 62600-200 from the IEC 2013. As required in that standard, the velocity signals are powered before temporal and spatial averaging for the computation of hydrodynamic coefficients. That averaging method, called power weighted average, is expressed in Eq. 1 with U_{ref} being either U_0 or U_S and n representing the number of samples in the temporal or the spatial spaces. The values of U_0 and U_S at the powers 1 to 3 are displayed in Tab. 1. We notice that, for the measurements in the undisturbed flow

9

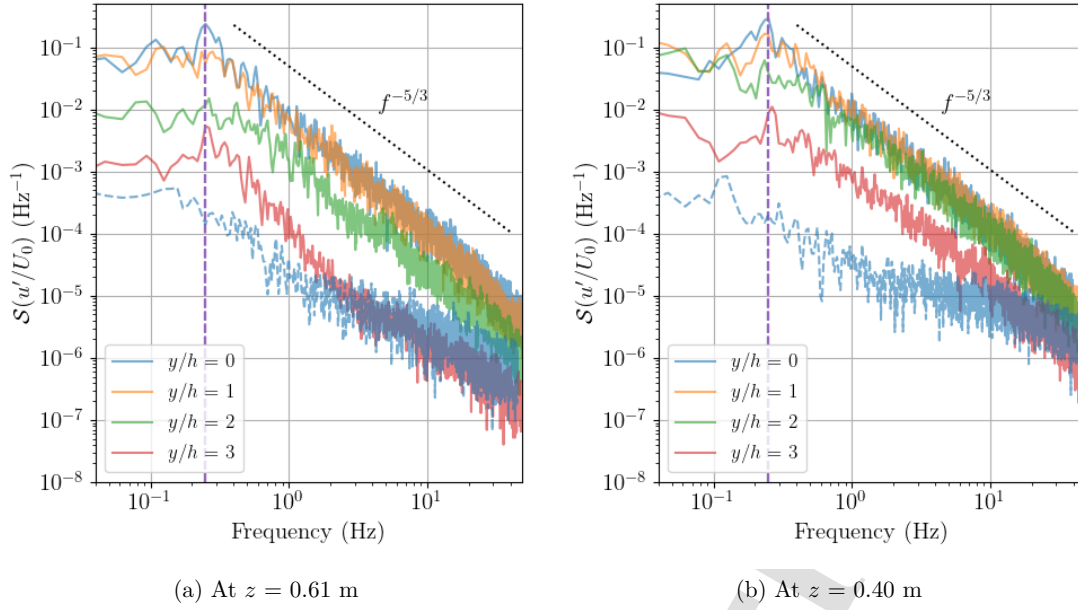(a) At $z = 0.61$ m   (b) At $z = 0.40$ m

Figure 10: Power spectral density of the fluctuating streamwise velocity measured by 3C-LDV. Solid lines are measurements behind the obstacle, without turbine, at $x = -H$ at the centre height of the top rotor (a) and of the bottom rotor (b). The blue dashed lines correspond to measurements in G0 without turbine at $y = 0$ and $z = 0.60$ m (a) and 0.40 m (b). The vertical dashed line indicates the vortices shedding frequency $f_u = 0.25$ Hz in the wake of the obstacle.

(U_S in G0 and U_0), the power weighted averages are equal to the arithmetic averages powered. However, in turbulent flows like in the wake of the bathymetry obstacle, the power weighted average gives higher values than the arithmetic average powered due to the flow fluctuation around the mean value (the arithmetic averages are not given here for clarity). In addition, we observe that the velocity averaged over the 2-VATT capture area U_S is 15 % lower in C6, in the wake of the bathymetry obstacle, than in G0, with a flat bathymetry.

$$U_{ref}^p = \frac{1}{n} \sum_n u^p \tag{1}$$

Table 1: Power weighted average reference velocities considered for the computation of the hydrodynamic coefficients in the two flow configurations.

	G0	C6
U_0 ($m.s^{-1}$)	0.944	
U_S ($m.s^{-1}$)	0.963	0.821
U_0^2 ($m^2.s^{-2}$)	0.891	
U_S^2 ($m^2.s^{-2}$)	0.928	0.709
U_0^3 ($m^3.s^{-3}$)	0.841	
U_S^3 ($m^3.s^{-3}$)	0.895	0.631

Considering either one or the other above mentioned reference velocities, the power coef-

10

ficient of each rotor column C_{Pcol} is computed as in Eq. 2 with $P_{col}(t) = Q(t)\omega(t)$ and t the time. The reference surface is that of the rotors projected area and the torque signal considered is corrected by the friction torque induced by the seals and the transmission system for each rotor column (Moreau et al. 2023a). Then, the overall average power coefficient $\overline{C_P}$ is the average of the two $C_{Pcol}(t)$ and the power fluctuation is analysed considering the average standard deviation between the two rotor columns, noted $\overline{\sigma}(C_{Pcol})$.

$$C_{Pcol}(t) = \frac{P_{col}(t)}{\rho D H_{blade} U_{ref}^3} \qquad (2)$$

In the same way, either with one reference velocity or the other, the tip speed ratio (λ) is defined in Eq. 3 and λ_{opt} refers to the operating point providing the maximal power coefficient. The force and moment coefficients are defined in Eq. 4 and 5 for the components along x with the four rotors projected area as a reference surface. They are defined the same way for the loads along y and z. The loads measured without current are subtracted to consider only the hydrodynamic loads on the device, without the gravity. Besides, in this study, we consider the forces applied by the turbine on the gravity base, measured by the upper load cell, and the moments measured at the bottom (Fig. 3 left). In addition to the load coefficients evolution with the tip speed ratio, we also analyse their probability density functions (PDF) with 50 equal-width bins to consider the loads repartition and look at their extrema.

$$\lambda(t) = \frac{\omega(t) R}{U_{ref}} \qquad (3)$$

$$C_x(t) = \frac{F_x(t)}{2\rho D H_{blade} U_{ref}^2} \qquad (4)$$

$$C_{Mx}(t) = \frac{M_x(t)}{2\rho R D H_{blade} U_{ref}^2} \qquad (5)$$

To deeper analyse the fluid-structure interaction, we compute the normalised cross-correlation $\mathcal{R}$ of some velocity components measured at $x = -H$ with some 2-VATT loads and with the torque of the rotor column facing the LDV probes (Eq. 6 where τ is the time lag). All the signals s are decomposed into $s = \overline{s} + s'$ with the bar indicating the average and the prime the fluctuating part of the signal. In this study, the cross-correlations are presented with three of the velocity components measured: u'_{2C}, u'_{3C} and w'_{3C}. Finally, the power spectral densities $\mathcal{S}$ of Q', F'_x and F'_z are computed using Welch's method with 64 s long windows and 50 % overlap to analyse the periodical characteristics of the 2-VATT related signals compared to those of the flow presented in Fig. 10.

$$\mathcal{R}\left(U', F'\right)[\tau] = \frac{\overline{\left(U(t) - \overline{U}\right)\left(F(t + \tau) - \overline{F}\right)}}{\sqrt{\overline{\left(U(t) - \overline{U}\right)^2} \ \overline{\left(F(t) - \overline{F}\right)^2}}} \qquad (6)$$

3 Bathymetry effects on the ducted 2-VATT behaviour

The effects of the bathymetry obstacle wake on the behaviour of the ducted 2-VATT are first analysed regarding the power performance of the turbine. We compare the effect between FC and EC as well as the effect of the reference velocity choice on the power coefficient. Then, we consider the effect of the bathymetry generated turbulence on the hydrodynamic load coefficients to discuss the risks of structural damage. Finally, the relations between the flow and the load fluctuation are assessed both in the temporal and the spectral domain.

11

3.1 Effects on the 2-VATT power performance

Fig. 11 (a) displays the average and the standard deviation of the power coefficient with regard to the tip speed ratio computed with U_0 in G0 and C6 with the 2-VATT either in the Flood Configuration or the Ebb Configuration. The results reveal that the average C_P curves drop, both in EC and FC, in C6 compared to G0 and that the differences between FC and EC in G0 remain in C6. Indeed, in C6 as in G0, the maximal $\overline{C_P}$ are rather equal given the measurement repeatability (Moreau et al. 2023a) and the optimal tip speed ratio is 0.1 lower in EC compared to FC. Besides, $\sigma(C_{Pcol})$ at λ_{opt} is more than doubled in C6 compared to G0 and the difference between FC and EC narrows in C6, showing that the turbulence affects more the fluctuating part of the turbine response than the relative counter-rotation direction of the two columns. In the following, we focus on the Flood tide Configuration to study the effect of the bathymetry obstacle wake on the behaviour of the 2-VATT.

Fig. 11 (b) presents the evolution of the power coefficient with regard to the tip speed ratio in FC in G0 and C6, depending on the reference velocity considered. On one hand, with U_S, the λ_{opt} are equal between G0 and C6 which means that the velocity field measured during a resource assessment at the turbine position (without it) is a good estimation of the velocity really perceived by the 2-VATT in operation. However, the maximal $\overline{C_P}$ is 16 % lower in C6 than in G0 with U_S as a reference velocity. With the velocity arithmetic average powered instead of the cubic power weighted average U_S as a reference in C6, $\max(\overline{C_P}/\overline{C_{Pmax}})$ would be 0.91 instead of the 0.79 in Fig. 11 (b). Thus, the decrease of $\overline{C_P}$ computed with U_S between G0 and C6 is mainly due to the higher level of turbulence in the wake of the bathymetry obstacle that increases the reference velocity due to the cubic weighted average of the velocity in the power coefficient computation. Part of the performance difference between G0 and C6 could also be due to a Reynolds number effect as U_S, and so the Reynolds number, is 15 % lower in C6 than in G0, which affects the blades lift and drag performance (Michna et al. 2022).

On the other hand, with U_0 as the reference velocity, the maximal $\overline{C_P}$ drops by 40 % between G0 and C6 and the optimal tip speed ratio is shifted from 1.6 to 1.4. That result shows that for a constant far upstream velocity, the hydrodynamic power really perceived by the turbine can significantly differ depending on the bathymetry shape between the velocity measurement point and the turbine (Mercier et al. 2022). Thus, in the perspective of tidal turbines monitoring at sea, the choice of the reference velocity measurement location is crucial to properly control the devices and analyse their performance. The latter conclusion is true for all bottom mounted tidal turbines, whatever their geometry. It is also instructive to notice that the little 2 % difference between U_0 and U_S values in G0 is responsible for the 6 % difference of the maximal $\overline{C_P}$. That result is due to the power 3 on U_{ref} in the computation of the power coefficient and shows once again the sensitivity of $\overline{C_P}$ to the reference velocity assessment.

Furthermore, the bathymetry obstacle wake also affects strongly the power fluctuation. First, the evolution with regard to λ is modified as $\overline{\sigma}(C_{Pcol})$ presents a maximum at $\lambda > \lambda_{opt}$ in C6 whereas the maximum is at low λ in G0. Then, and more challenging, $\overline{\sigma}(C_{Pcol})$ is multiplied by 3.1 at λ_{opt} when considering the constant far upstream velocity U_0 and by 5.4 when considering the velocity really perceived by the turbine U_S. That power fluctuation is due to a 3.8 times greater torque standard deviation at the optimal operating point in C6 compared to G0. The fluctuation intensity (standard deviation divided by average, FI) of the torque at λ_{opt} is 1.43 in C6 against 0.24 in G0, as a consequence of both the increased standard deviation and the decreased average. We also observe a 3.0 times higher standard deviation of the rotational speed at λ_{opt}, although $FI(\omega)$ is only 0.002 and 0.006 in G0 and C6 resp. given the motors control at constant speed. That small temporal scale fluctuation of the power generation when the tidal turbine is in the wake of a large bathymetry obstacle must be taken into account in the design of the electricity conversion system to provide a smooth signal to the grid.

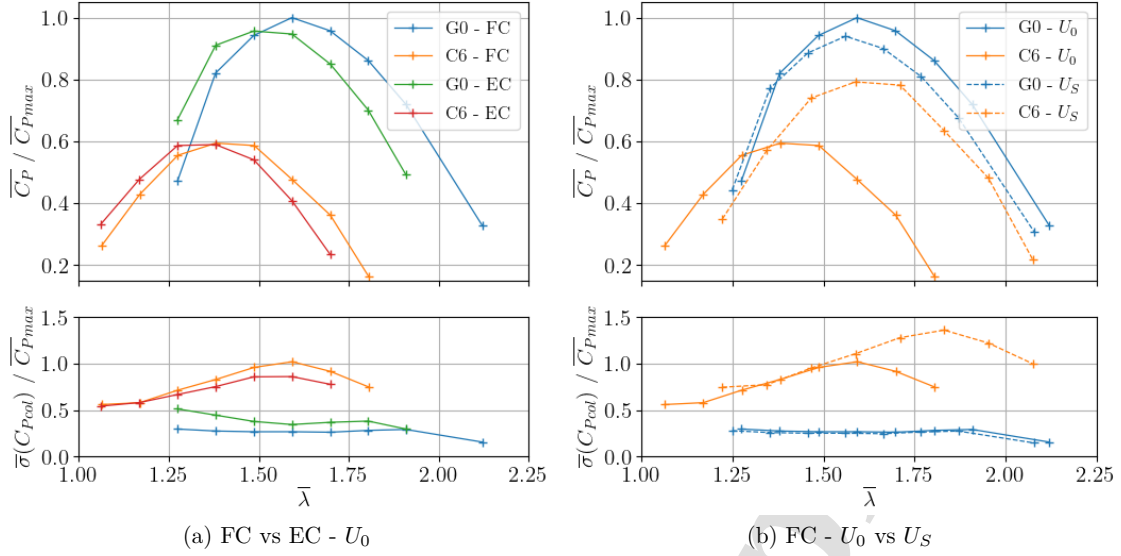(a) FC vs EC - U_0 (b) FC - U_0 vs U_S

Figure 11: Average and standard deviation of the power coefficient with regard to the tip speed ratio in G0 and C6. (a) $C_P(U_0)$ in the Flood and Ebb tide Configurations. (b) $C_P(U_0)$ and $C_P(U_S)$ in FC only. The values are normalized by the maximal $\overline{C_P(U_0)}$ in G0 - FC.

3.2 Effects on the loads applied to the 2-VATT

Fig. 12 presents the average and the standard deviation of the drag (a) and the lift (b) coefficients computed either with U_S or U_0 both in G0 and C6. Similarly to the power coefficient, the presence of the bottom mounted obstacle leads to a 23 % drop of $\overline{C_x}$ computed with U_0 between G0 and C6 due to the decreased velocity in the wake of the bathymetry obstacle. It is worth noting that, at λ_{opt}, 60 % of the turbine drag is due to the rotors thrust while the other 40 % is due to the static structure drag (Moreau et al. 2023a). Computed with U_S, the $\overline{C_x}$ values are of the same order of magnitude in G0 and C6, indicating no effect of the turbulence and the flow shear on the average drag coefficient. However, the drag standard deviation is multiplied by 2 at λ_{opt} in C6 compared to G0. The results on C_{My} are the same as on C_x but the effect of the bathymetry obstacle wake on the vertical load applied to the 2-VATT is different (Fig. 12 (b)). Indeed, $\overline{C_z}$ is more than 2.5 times lower in C6 compared to G0, independently from the reference velocity. This result means that the turbine apparent weight on the base is higher when the 2-VATT is in the wake of that bathymetry obstacle compared to the flat floor configuration. We explain this result by the negative vertical velocity field, up to $w = -0.1U_0$, measured in the wake of the bottom mounted cylinder near the turbine position (Fig. 8). Conversely, the vertical load fluctuation is strongly increased by the presence of the bathymetry obstacle upstream as $\sigma(C_z)$ is multiplied by 10 between G0 and C6 at λ_{opt} with U_S as the reference velocity. Similarly to the torque fluctuation intensity, the difference in $FI(C_z)$ is even bigger than in $\sigma(C_z)$ as the average vertical load decreases while its standard deviation increases. Thus, $FI(C_z)$ is less than 10 % in G0 whereas it is more than 200 % in C6, both with U_0 and U_S at λ_{opt}.

To investigate further the effect of the bathymetry obstacle wake on the 2-VATT load fluctuation, we compute the probability density functions (PDF) of the 6 load components. Fig. 13 presents the PDF of the 3 force coefficients (a) and of the 3 moment coefficients at the bottom of the base (b) in G0 and C6 at λ_{opt}. Here, the coefficients are computed with U_0 to analyse the effect of the bathymetry-modified flow on the loads for a given far upstream hydrodynamic power potential. The results show that, for all of the 6 load components, the

13

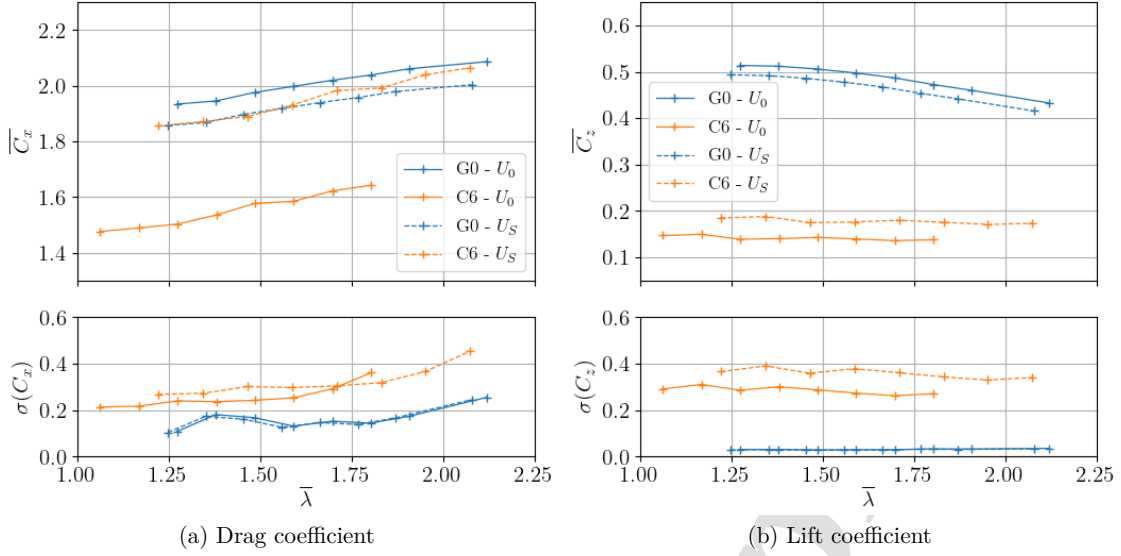(a) Drag coefficient

(b) Lift coefficient

Figure 12: Average (top) and standard deviation (bottom) of the drag and lift coefficients with regard to the tip speed ratio in G0 and C6 computed with either U_0 or U_S.

range between the minimum and maximum values are significantly wider in C6 than in G0, which is due to the wider velocity range induced by the turbulence in the wake of the bathymetry obstacle (Fig. 9). As a consequence, the fatigue stress of the 2-VATT structure is increased (Milne et al. 2010). In addition, C_x and C_{My} reach the highest absolute values among the 6 load components, placing them as the most critical quantities for the drifting and overturning risk considerations at the gravity base design stage. It appears that their maximal values in C6 are lower than those in G0. Thus, for a given far upstream velocity, the drifting and overturning risks are lowered by the presence of a wide bathymetry obstacle upstream of the 2-VATT. To moderate that conclusion, Fig. 13 (a) also shows that, despite the decrease of C_z average, its maximal values are approximately doubled in the configuration C6 compared to G0. That result means that, in some extreme cases, the apparent weight of the turbine on the base is lightened by the incident flow, which lowers the device resistance to the drifting. Thus, the occurrence of maximal C_z simultaneously with maximal C_x could increase the drifting risk. Finally, the transverse forces and moments maximal values are all overtopped, probably due to the instantaneous flow asymmetries induced by the coherent flow structures.

Independently from the flow characteristics, the PDF shapes are affected by the (random) relative phase of the two rotor columns since the loads are measured on the whole turbine. Among several repetitions of the same operating point in G0, we observe that when the two columns are rather in phase (i.e. when the blades absolute positions are symmetrical), the C_x and C_{My} PDF present two maxima, whereas they have a single maximum when the rotor columns are rather out of phase (Fig. 14). In addition when the rotors are parked, the 6 loads PDF are narrower and they present a single maximum. We suggest that the presence of two C_x (and C_{My}) PDF maxima at λ_{opt} corresponds to the cases when the two phased columns are either at a maximum or at a minimum of torque generation, inducing two mostly probable C_x values on each side of the average value. Whereas the presence of a single C_x PDF maximum could mean that the torque fluctuation of one rotor column is compensated by the other out of phase column, which smooths the overall C_x signal and provides a single maximum of probability at the average coefficient value. The number of maxima in C_y and C_{Mx} PDF is opposed to that of C_x and C_{My}. This can be explained by an analogous reflection on

14

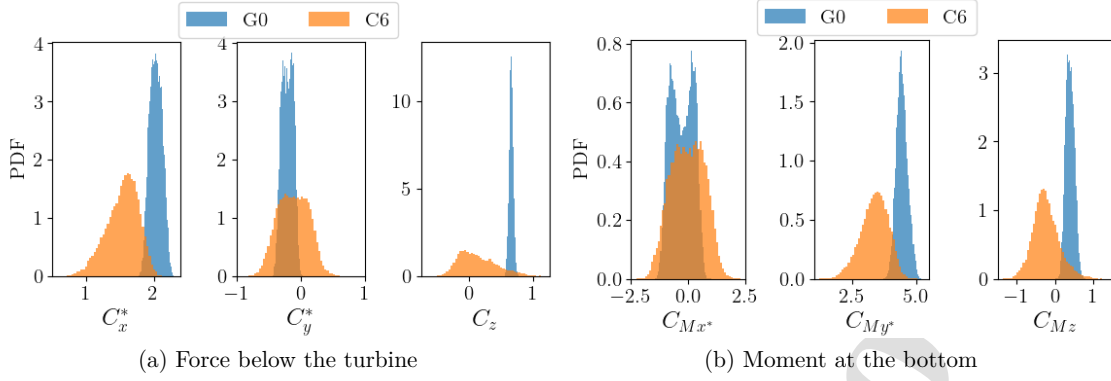(a) Force below the turbine

(b) Moment at the bottom

Figure 13: Probability Density Functions of the load coefficients computed with U_0 in G0 and C6.

the balancing of the fluctuating lateral loads generated by the two vertical axis rotor columns, whether in phase or out of phase. When comparing the loads between the C6 and the G0 configurations (Fig. 13), we chose to present the loads PDF for the repetition cases when the two columns are rather out of phase in the two flow conditions. That being, the conclusions regarding the effect of the bathymetry-generated turbulent flow on the 2-VATT compared to the flat bed configuration remain, as the load ranges in C6 largely exceed those in G0, regardless of the rotor column phasing.

(a) Force below the turbine

(b) Moment at the bottom
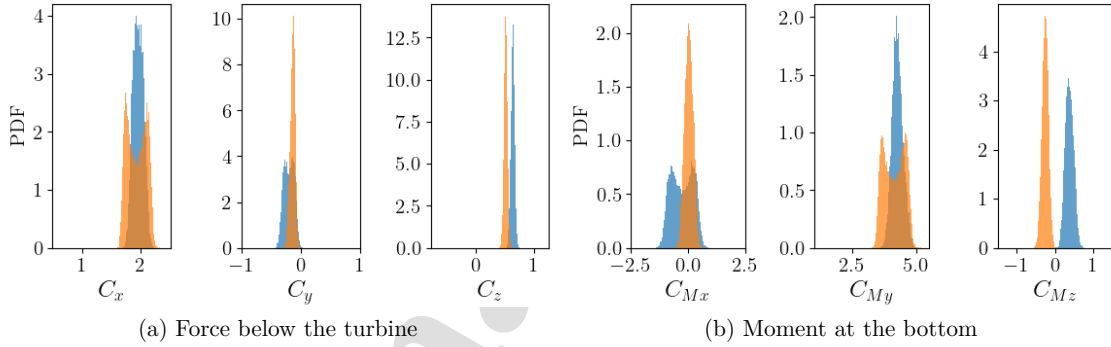
Figure 14: Probability Density Functions of the load coefficients computed with U_0 at λ_{opt} in G0 when the two rotor columns are rather in phase (orange) or out of phase (blue).

The two last sections showed a significant increase of both the power and the load fluctuation when the bottom mounted 2-VATT is placed in the wake of a wide bathymetry obstacle compared to the configuration with a flat bathymetry. In the following section, we focus on that fluctuation origin through analyses in the temporal and in the spectral domain.

3.3 Fluid induced torque and load fluctuation

Fig. 15 displays the cross-correlation of the fluctuating torque of the red column Q'_R, the drag force F'_x and the lift force F'_z with the fluctuating velocity components measured at $x = -H$ by the 2C- and 3C-LDV in front of the top and bottom rotors respectively. The results at λ_{opt} show a maximum of correlation close from 0.4 between the drag and the two streamwise velocity measurements. However, the lag at which the maxima occur are -0.45 s with u'_{2C} against -0.75
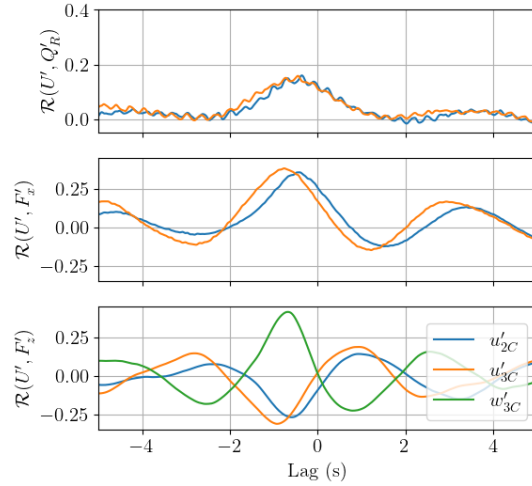
15

Figure 15: Cross-correlation of the fluctuating torque Q'_R of the red column, the drag force F'_x and the lift force F'_z with the fluctuating velocity components measured at $x = -H$ by the 2C- and 3C-LDV in front of the top and bottom rotors respectively. The blue and orange curves are correlations with the streamwise velocity whereas the green one is with the vertical velocity component.

s with u'_{3C} while the maximum of the cross-correlation between u'_{2C} and u'_{3C} occurs at $\tau = 0$ s. This difference of lag is simply explained by the shear in the bathymetry obstacle wake that provides a faster transport of the flow fluctuation towards the turbine at the height of the 2C-LDV probe (top rotor) than at the height of the 3C-LDV probe (bottom rotor). Besides, the results on the lift reveal a negative correlation with the streamwise velocities and a stronger positive correlation with the vertical velocity fluctuation w'. Overall, those lift and drag results feed the discussion on the drifting risk as they mean that peaks of w generate peaks of F_z whereas peaks of u produce peaks of F_x but troughs of F_z. Therefore, maxima of F_z cannot occur simultaneously with maxima of F_x and so the device drifting risk is actually decreased by the presence of the bathymetry obstacle for a given far upstream velocity. Fig. 15 also reveals that the lag at the maximum torque correlation with the streamwise velocity is equal for the two velocities considered despite the flow shear, in opposition to the results on the lift and drag forces. That maximum torque correlation lag is the same as the one of the drag with the 2C-LDV measurement (top rotor), which indicates that the whole rotor column response is dominated by the response of the top rotor. In an undisturbed flow, the authors already found that the top rotor dominates the torque generation when the 2-VATT faces a sheared velocity profile (Moreau et al. 2023b) as it is the case in the cylinder wake. We also observe that the maximum of torque correlation at λ_{opt} is less than 0.5 times that of the drag, indicating that the flow fluctuation impact is lesser on the 2-VATT rotating parts than on the overall structure.

Furthermore, $\mathcal{R}(U', Q'_R)$ presents high frequency oscillations and the loads correlations show secondary maxima with about 4 s lag compared to the absolute maxima, which indicates related periodical fluctuation of the flow and the loads. To better characterise that periodical fluctuation, Fig. 16 displays the torque, drag and lift power spectral densities $\mathcal{S}$. First, we can observe that the overall amplitude of the three spectra is about 10 times higher in C6 than in G0, up to about $f_c = 4\text{-}5$ Hz on the loads and on the whole frequency range for the torque. This result is in line with the higher levels of the velocity spectra observed in the wake of the bathymetry obstacle compared to the flat bathymetry configuration (Fig. 10). The frequency at which the loads spectra level in C6 reach the level of G0 indicates that the 2-
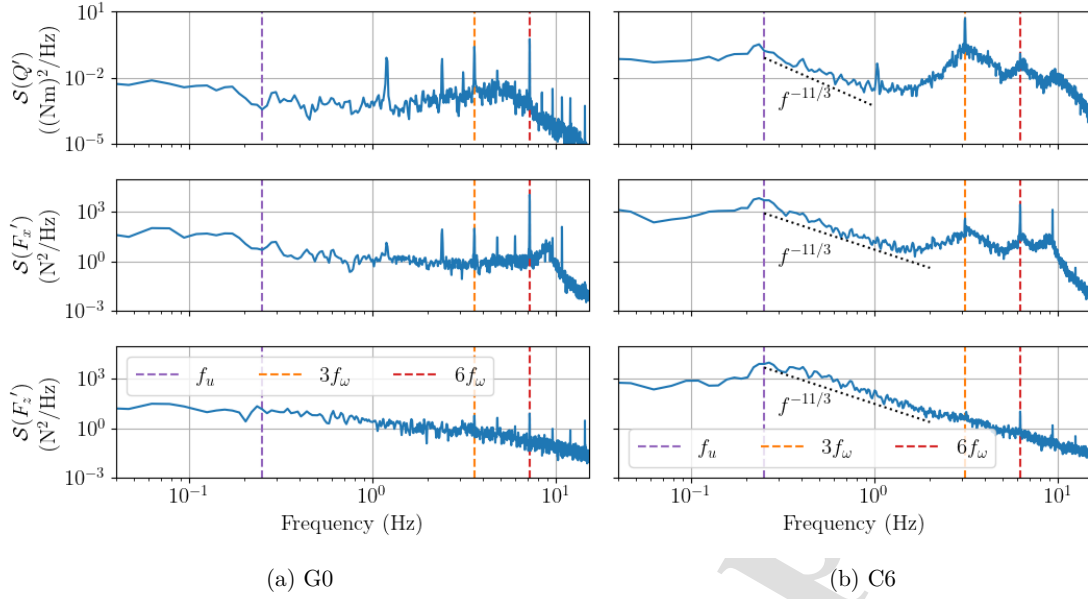
16

(a) G0   (b) C6

Figure 16: Power spectral density of the fluctuating torque Q' (top), the drag force F_x' (middle) and the lift force F_z' (bottom) at λ_{opt} in G0 (left) and C6 (right). f_ω is 1.20 Hz in G0 against 1.04 Hz in C6 at λ_{opt} due to the difference of U_S.

VATT is insensitive to higher frequency turbulence. Considering the surface averaged velocity U_S in C6, we deduce that the 2-VATT drag and lift are sensitive to turbulence structures whose characteristic length l is greater than $l = U_S/f_c \simeq 0.2$ m, which is between $H/2$ and $H/3$. That critical size of turbulent structure is consistent with the observations on HATTs (Chamorro et al. 2015; Gaurier et al. 2020b). The rotors projected area being smaller than the overall structure, the torque response is indeed impacted by smaller turbulence structures revealed by the higher $\mathcal{S}$ level in C6 on the whole frequency range.

Then, on one hand, between 1 and 10 Hz, $\mathcal{S}(Q')$ in C6 is dominated by a peak at 3 times the rotational frequency (f_ω) despite the 6 blades that compose the rotor column. Indeed, the peak amplitude at $3f_\omega$ is about 40 times higher than the one at $6f_\omega$. Fig. 8 shows that the flow is strongly sheared behind the bathymetry obstacle and the authors previously found that the torque spectral peak at $3f_\omega$ becomes stronger relatively to the one at $6f_\omega$ in presence of a sheared flow as the bottom rotor contribution to the whole column torque diminishes (Moreau et al. 2023b). By comparing Fig. 10 (a) and (b), we also observe that the higher levels of torque and loads spectra in C6 exceeds the level of most of the rotational frequency harmonics observed in G0. As a consequence, only the 1st, 3rd, 6th and 9th harmonics can be observed in C6 spectra. On the other hand, between 0.1 and 1 Hz, the loads spectra in C6 are dominated by a frequency peak around $f_u = 0.25$ Hz which carries more power than the lower frequencies and than the rotational frequency harmonics. Those low frequency peaks are absent in G0. The velocity spectra behind the bathymetry obstacle presented in Fig. 10 also display large peaks around that frequency and was found to be due to the coherent turbulent structures shedding in the obstacle wake (Ikhennicheu et al. 2019b). Thus, the present results show that the load fluctuation is more affected by the periodical impacts of the vortices on the structure than by the blades rotation. However, that flow induced spectral response around f_u is a lot weaker in the torque spectra as its power is about 15 times lower than that at $3f_\omega$. From the flow spectra in Fig. 10, it appears that the high energy vortices are mainly located at the centre of the tank ($y/h = 0$), which is also the centre of the obstacle and of the 2-VATT; but

17

the vortices signature around f_u is barely visible at $y/h = 1$ and 2 and appears again at $y/h = 3$ with about 50 times less power than at $y/h = 0$. Consequently, the high energy vortices impact the central fairing of the ducted 2-VATT, which explains the high spectral content on the lift and drag at the vortex shedding frequency. However, the rotors, located between $y/h = 0.5$ and 2, are away from the most energetic vortices path, which explains the relatively low spectral content on the rotor torque at the vortex shedding frequency. Thus, the torque and so the power fluctuation rise in the wake of the bathymetry obstacle are mostly due to the flow shear that unbalances the contribution of the upper and lower rotors, and by the coherent flow structures to a lesser extent. Finally, although the VATT blades sweep a 3-dimensional surface by opposition to those of a HATT which sweep a 2-dimensional disc, the torque and load spectra also decay following a -11/3 power law in the turbulent bottom-mounted obstacle wake (Druault et al. 2022).

4 Conclusion

This paper aims at studying the response of a ducted bottom-mounted twin vertical axis tidal turbine (2-VATT) placed in the wake of a wide bathymetry obstacle. To do so, we tested a 1/20 scale model of such a 2-VATT in Ifremer's tank either on a flat bed (configuration G0) or downstream of a wide bottom-mounted square cylinder (configuration C6) and we measured the turbine response simultaneously with the flow velocity. The wake of that obstacle is characterised by a strong velocity shear, both vertically and laterally, a high level of turbulence with an average turbulence intensity above 25 % on the 2-VATT capture area, and the shedding of large coherent flow structures every 4 s. Those scaled flow characteristics are similar to what can be measured in offshore tidal energy sites with uneven sea beds. The main results of our study are what follows.

First, it appears that the reference velocity chosen to compute the average power and loads coefficients strongly influences the results. On one hand, considering a constant far upstream velocity as a reference, regardless of the bathymetry between the measurement point and the turbine, the presence of a wide bathymetry obstacle upstream of the 2-VATT leads to a 40 % average power loss compared to the flat bed case. That result highlights mainly the effect of the velocity deficit in the obstacle wake. On the other hand, considering the velocity really perceived by the 2-VATT in the two bathymetry configurations, *i.e.* the power weighted average velocity at the device location prior to its installation, the power coefficient appears just 16 % lower in C6 than in G0. That result is partly due to the higher levels of turbulence in the wake of the bathymetry obstacle that increases the reference velocity value due to the cubic weighted average and probably to some Reynolds number effects.

In addition, we observe that the power standard deviation is more than 3 times higher in C6 than in G0 which is due to a similar increase of the torque fluctuation. The spectral analysis of the torque signal reveals that its fluctuation in C6 are mostly due to the strong vertical flow shear (as shown in Fig. 8), and to the passing of coherent flow structures to a lesser extent.

Then, regarding the 2-VATT loads for a given far upstream velocity, the average hydro-dynamic coefficients are lower in C6 than in G0 but their probability density functions are substantially wider, indicating larger fluctuation. That fluctuation is directly due to coherent structures passing as the loads spectral content is dominated by a peak at the coherent structures shedding frequency in the bathymetry obstacle wake. Quantitatively, the drag and lift standard deviations are multiplied by 2 and 10 respectively. The high fluctuation rates of the loads must be considered in the design of the structure for fatigue considerations. However, the maximal drag and pitch values in C6 remain below those in G0, so the 2-VATT drifting and overturning risks are not exceeded when the device is downstream of a wide bathymetry obstacle. These loadings can be further reduced thanks to a modification of the turbine design

18

as shown in Saouli et al. 2023 which presents a comparison of two twin vertical axis tidal turbine designs showing how an unducted design can improve the loading distribution and turbine response under waves sollicitation.

In a previous study, we tested two types of bathymetry obstacles with two obstacle-to-turbine distances for each (Bloch et al. 2022). That study revealed that the C6 configuration was the most impacting on the turbine behaviour among the 4 bathymetry obstacle configurations tested. Indeed, the 2-VATT power and load fluctuation is less intense, although significantly stronger than in the flat bed configuration, when it is located further downstream of the square cylinder or when the bathymetry obstacle is a combination of a cube with the square cylinder. In future works, we could conduct an analysis similar to that of the present paper regarding the effect of the combined cube and cylinder wake on the 2-VATT behaviour as the wake structure of that combination differs from the single cylinder case (Magnier et al. 2021).

In the light of these results, the authors recommend to carefully consider the bathymetry of each high potential tidal energy site not only for laying considerations but also to avoid lower velocity (and so power) areas due to upstream bathymetric singularities. In addition, the flow characterisation at the precise projected location of each turbine should be carried out as early as possible in the project timeline to qualify the site specific velocity probability density functions and design appropriate fatigue-proof structures. Finally, the choice of the upstream velocity measurement location(s) for the tidal turbines monitoring and performance assessment should also carefully consider the bathymetry to provide a relevant reference of the incident hydrodynamic power. The quite large area indicated as suitable by the IEC TS 62600-200 for current profiler placement to measure the incident resource at sea may need to be refined regarding the upstream bathymetry (IEC 2013).

5   Acknowledgements

References

Ahmadi-Baloutaki, M., R. Carriveau, and D. S. Ting (2015). "Performance of a vertical axis wind turbine in grid generated turbulence". In: *Sustainable Energy Technologies and Assessments* 11, pp. 178–185. DOI: 10.1016/j.seta.2014.12.007.

Bloch, N., M. Moreau, G. Germain, and G. Maurice (2022). "Experimental study of bathymetry variation effects on a cross-flow water turbine". In: *18èmes Journées de l'Hydrodynamique*. Poitiers, pp. 1–12. URL: https://jh2022.sciencesconf.org/413851.

Chamorro, L. P., C. Hill, V. S. Neary, B. Gunawan, R. E. A. Arndt, and F. Sotiropoulos (2015). "Effects of energetic coherent motions on the power and wake of an axial-flow turbine". In: *Physics of Fluids* 27.5, p. 055104. DOI: 10.1063/1.4921264.

Cossu, R., I. Penesis, J.-R. Nader, P. Marsh, L. Perez, C. Couzi, A. Grinham, and P. Osman (2021). "Tidal energy site characterisation in a large tidal channel in Banks Strait, Tasmania, Australia". In: *Renewable Energy* 177, pp. 859–870. DOI: 10.1016/j.renene.2021.05.111.

Druault, P., B. Gaurier, and G. Germain (2022). "Spatial integration effect on velocity spectrum: Towards an interpretation of the -11/3 power law observed in the spectra of turbine outputs". In: *Renewable Energy* 181, pp. 1062–1080. DOI: 10.1016/j.renene.2021.09.106.

Furgerot, L., A. Sentchev, P. Bailly du Bois, G. Lopez, M. Morillon, E. Poizot, Y. Méar, and A. C. Bennis (2020). "One year of measurements in Alderney Race: preliminary results from database analysis". In: *Philosophical transactions. Series A, Mathematical, physical, and engineering sciences* 378.2178, p. 20190625. DOI: 10.1098/rsta.2019.0625.

Gaurier, B., P. Druault, M. Ikhennicheu, and G. Germain (2020a). "Experimental analysis of the shear flow effect on tidal turbine blade root force from three-dimensional mean flow reconstruction: Shear flow effect on tidal turbine blade". In: *Philosophical Transactions of the Royal Society A: Mathematical, Physical and Engineering Sciences* 378.2178. DOI: 10.1098/rsta.2020.0001.

Gaurier, B. (2020). "Etude expérimentale des performances d'une hydrolienne, soumise aux effets de la turbulence et de l'intéraction houle-courant". PhD thesis. Normandie Université. URL: https://tel.archives-ouvertes.fr/tel-03030615.

Gaurier, B., G. Germain, J.-V. Facq, and T. Bacchetti (2018). *Wave and current flume tank of IFREMER at Boulogne-sur-mer. Description of the facility and its equipment.* Tech. rep. IFREMER. DOI: 10.13155/58163.

Gaurier, B., M. Ikhennicheu, G. Germain, and P. Druault (2020b). "Experimental study of bathymetry generated turbulence on tidal turbine behaviour". In: *Renewable Energy* 156, pp. 1158–1170. DOI: 10.1016/j.renene.2020.04.102.

Gooch, S., J. Thomson, B. Polagye, and D. Meggitt (2009). "Site characterization for tidal power". In: *OCEANS 2009.* IEEE, pp. 1–10. DOI: 10.23919/OCEANS.2009.5422134.

Grondeau, M., S. Guillou, P. Mercier, and E. Poizot (2019). "Wake of a ducted vertical axis tidal turbine in turbulent flows, LBM actuator-line approach". In: *Energies* 12.22, p. 4273. DOI: 10.3390/en12224273.

IEC (2013). "Technical specification 62600-200: Electricity producing tidal energy converters – Power performance assessment". In: *Marine energy – Wave, tidal and other water current converters.* International Electrotechnical Commission.

Ikhennicheu, M., G. Germain, P. Druault, and B. Gaurier (2019a). "Experimental investigation of the turbulent wake past real seabed elements for velocity variations characterization in the water column." In: *International Journal of Heat and Fluid Flow* 78. DOI: 10.1016/j.ijheatfluidflow.2019.108426.

— (2019b). "Experimental study of coherent flow structures past a wall-mounted square cylinder". In: *Ocean Engineering* 182.May, pp. 137–146. DOI: 10.1016/j.oceaneng.2019.04.043.

Lucas, N. S., M. J. Austin, T. P. Rippeth, B. Powell, and P. Wakonigg (2022). "Turbulence and coherent structure characterisation in a tidally energetic channel". In: *Renewable Energy* 194, pp. 259–272. DOI: 10.1016/j.renene.2022.05.044.

Magnier, M., P. Druault, and G. Germain (2021). "Experimental investigation of upstream cube effects on the wake of a wall-mounted cylinder: Wake rising reduction, TKE budget and flow organization". In: *European Journal of Mechanics - B/Fluids* 87.June, pp. 92–102. DOI: 10.1016/j.euromechflu.2021.01.004.

Mercier, P. and S. S. Guillou (2022). "Spatial and temporal variations of the flow characteristics at a tidal stream power site: A high-resolution numerical study". In: *Energy Conversion and Management* 269.May, p. 116123. DOI: 10.1016/j.enconman.2022.116123.

Mercier, P. and S. Guillou (2021). "The impact of the seabed morphology on turbulence generation in a strong tidal stream". In: *Physics of Fluids* 33.5, p. 055125. DOI: 10.1063/5.0047791.

Mercier, P., M. Ikhennicheu, S. Guillou, G. Germain, E. Poizot, M. Grondeau, J. Thiébot, and P. Druault (2020). "The merging of Kelvin–Helmholtz vortices into large coherent flow structures in a high Reynolds number flow past a wall-mounted square cylinder". In: *Ocean Engineering* 204.March, p. 107274. DOI: 10.1016/j.oceaneng.2020.107274.

Michna, J. and K. Rogowski (2022). "Numerical Study of the Effect of the Reynolds Number and the Turbulence Intensity on the Performance of the NACA 0018 Airfoil at the Low Reynolds Number Regime". In: *Processes* 10.5, p. 1004. DOI: 10.3390/pr10051004.

Milne, I. A., R. N. Sharma, R. G. Flay, and S. Bickerton (2010). "The role of onset turbulence on tidal turbine blade loads". In: *17th Australasian Fluid Mechanics Conference* December, pp. 444–447. URL: https://flair.monash.edu.au/intranet/proceedings/17afmc{_}proceedings/PDF/093{_}Paper.pdf.

Möllerström, E., F. Ottermo, A. Goude, S. Eriksson, J. Hylander, and H. Bernhoff (2016). "Turbulence influence on wind energy extraction for a medium size vertical axis wind turbine". In: *Wind Energy* 19.11, pp. 1963–1973. DOI: 10.1002/we.1962.

Moreau, M., G. Germain, and G. Maurice (2023a). "Experimental performance and wake study of a ducted twin vertical axis turbine in ebb and flood tide currents at a 1/20th scale". In: *Renewable Energy* 214, pp. 318–333. DOI: 10.1016/j.renene.2023.05.125.

— (2023b). "Misaligned sheared flow effects on a ducted twin vertical axis tidal turbine". In: *Applied Ocean Research* 138, p. 103626. DOI: 10.1016/j.apor.2023.103626.

Moreau, M., G. Germain, G. Maurice, and A. Richard (2022). "Sea states influence on the behaviour of a bottom mounted full-scale twin vertical axis tidal turbine". In: *Ocean Engineering* 265, p. 112582. DOI: 10.1016/j.oceaneng.2022.112582.

Naberezhnykh, A., D. Ingram, and I. Ashton (2023). "Wavelet applications for turbulence characterisation of real tidal flows measured with an ADCP". In: *Ocean Engineering* 270.January, p. 113616. DOI: 10.1016/j.oceaneng.2022.113616.

Ouro, P., P. Dené, P. Garcia-Novo, T. Stallard, Y. Kyozuda, and P. Stansby (2022). "Power density capacity of tidal stream turbine arrays with horizontal and vertical axis turbines". In: *Journal of Ocean Engineering and Marine Energy*. DOI: 10.1007/s40722-022-00257-8.

Ouro, P. and T. Stoesser (2019). "Impact of Environmental Turbulence on the Performance and Loadings of a Tidal Stream Turbine". In: *Flow, Turbulence and Combustion* 102.3, pp. 613–639. DOI: 10.1007/s10494-018-9975-6.

Peng, H. and H. Lam (2016). "Turbulence effects on the wake characteristics and aerodynamic performance of a straight-bladed vertical axis wind turbine by wind tunnel tests and large eddy simulations". In: *Energy* 109, pp. 557–568. DOI: 10.1016/j.energy.2016.04.100.

Saouli, Coquet, Facq, Gaurier, G. Germain, Gomez, Marcon, Maurice, and Moreau (2023). "Experimental comparison of the flow-induced loading between a ducted bottom-mounted twin vertical axis tidal turbine at still and an unducted prototype". In: *Proceedings of the European Wave and Tidal Energy Conference* 15. DOI: 10.36688/ewtec-2023-498. URL: https://submissions.ewtec.org/proc-ewtec/article/view/498.

Thiébaut, M., J.-F. Filipot, C. Maisondieu, G. Damblans, C. Jochum, L. F. Kilcher, and S. Guillou (2020). "Characterization of the vertical evolution of the three-dimensional turbulence for fatigue design of tidal turbines". In: *Philosophical Transactions of the Royal Society A: Mathematical, Physical and Engineering Sciences* 378.2178, p. 20190495. DOI: 10.1098/rsta.2019.0495.

Highlights

- Vertical axis turbine in the wake of uneven bathymetry generating flow variation
- Obstacle wake induces strong drop in the average power and loads coefficients
- Sheared flow and turbulence extend the torque and power fluctuations.
- Coherent flow structures induce load fluctuations.

Declaration of interests

X The authors declare that they have no known competing financial interests or personal relationships that could have appeared to influence the work reported in this paper.

☐The authors declare the following financial interests/personal relationships which may be considered as potential competing interests: